International Journal of Mechanical Sciences 194 (2021) 106186

Contents lists available at ScienceDirect

International Journal of Mechanical Sciences

journal homepage: www.elsevier.com/locate/ijmecsci

A multiscale simulation approach to grinding ferrous surfaces for process optimization

S.J. Eder[a,b,*], S. Leroch[a], P.G. Grützmacher[b], T. Spenger[c], H. Heckes[d]

[a] AC2T research GmbH, Viktor-Kaplan-Straße 2/C, 2700 Wiener Neustadt, Austria
[b] Institute of Engineering Design and Product Development, TU Wien, Lehárgasse 6 — Objekt 7, 1060 Vienna, Austria
[c] Institute of Production Engineering, Graz University of Technology, Kopernikusgasse 24/I, 8010 Graz, Austria
[d] Tyrolit – Schleifmittelwerke Swarovski K.G., Swarovskistraße 33, 6130 Schwaz, Austria

ARTICLE INFO

Keywords:
Grinding
Large-scale molecular dynamics
Material point method
Surface quality
Microstructure

ABSTRACT

A fundamental optimization of a grinding process usually involves expensive equipment and experimental matrices covering a large parameter space. To aid this often cumbersome procedure, here we present three simulation approaches that are intrinsically related and even use the same software, but consider the grinding process at different levels of detail, thus spanning several length scales. Using a molecular dynamics (MD) model, we subject a nanocrystalline carbon steel work piece to grinding by hard alumina abrasives and study material removal and surface topography. A second, much larger MD model allows us to additionally study the microstructural and stress response of a polycrystalline ferritic work piece with a grain size that qualitatively reproduces macroscopic material behavior. Finally, the material point method is introduced as a way of modeling a machining process at the mesoscale in a mesh-free fashion, which is highly advantageous because it intrinsically treats the large deformations during chip formation correctly without the need for repeated remeshing. We discuss which aspects of the grinding process or the work piece quality may be optimized using the adopted approaches, and we show that although our simulations span almost four orders of magnitude in length, the obtained material removal rates agree well. Thus, the presented mesh-free multiscale approach opens new avenues for simulation-aided optimization of grinding processes.

1. Introduction

In the course of finishing of hardened components, machining processes like grinding are often the only mechanical processing option able to meet the precision requirements in terms of geometric shape, dimensions and surface quality [1]. Ground areas of a work piece commonly represent its final surface [2], which is why it is necessary to maintain small tolerance fields with regard to topographic deviations and defects during the machining process. As component functionality and quality are both highly influenced in this final machining step, it is important to avoid process errors, which are associated with high costs [3]. Improved grinding technology allows high quality to be achieved for a variety of applications, e.g., precision-finished gears, while maintaining high productivity, which is why continuous development remains necessary throughout the production environment [4]. Mostly, grinding processes are optimized towards geometric shape of the work piece and its surface quality. However, additional attributes and effects also have to be considered when choosing the combined set of grinding parameters and tool choices since these can significantly influence the material properties and may lead to differences in efficiency and durability [5–7]. These additional attributes include, but are not limited to, heat levels, stresses, (re)crystallization, and chemical reactions, which influence the material properties and may lead to differences in efficiency and durability [8]. The choice of grinding parameters and tool, may affect the quality of a work piece. Thereby, the quality can be improved considerably with the correct choice of the parameters and vice versa. Therefore, it is highly beneficial to first understand the effect of grinding parameters and tool on the resulting geometry, surface quality, and material properties to then gain control over these impacts. There is already well-established knowledge about certain parameters that critically affect material properties: predominantly, there are pressure and heat [9]. In terms of pressure it has been shown that an increase in pressure results in higher grinding efficiency but lower surface quality (i.e., surface roughness, surface hardness, residual stresses, grain growth) [10,11]. High temperatures occurring during the grinding process may lead to grain growth and softening of the near-surface zones, phase transformations, burning, and cracks [2,9,12]. Moreover, variations in pressure and temperature also considerably affect chip morphology. Therefore, many experiments have already been conducted to understand the systems behind chip formation, including geometrical influences like the undeformed chip thickness [13], shearing and tip angles as well as cut-

* Corresponding author.
E-mail address: stefan.eder@ac2t.at (S.J. Eder).

https://doi.org/10.1016/j.ijmecsci.2020.106186
Received 4 September 2020; Received in revised form 9 October 2020; Accepted 2 November 2020
Available online 5 November 2020

ting velocities [14] and relating to those, the specific material removal rates of a system. However, these influences are not the singular source defining chip formation [15]. The work piece material itself additionally significantly affects chip formation as this is also critically influenced by the material properties such as density, elasticity, hardness, or heat capacity [16]. Furthermore, the material properties close to machined surfaces may also differ significantly from the bulk, due to considerable changes in the near-surface microstructure (specifically grain fining or coarsening), that occur during the machining process [17,18]. The resulting changes are barely or not at all noticeable using regular quality measures, making it even more critical to have a good understanding of such effects even before any *in-situ* trial is to be conducted.

As an element to aid the achievement of the topographic and near-surface microstructural qualities required by industry [19,20], simulations constitute a powerful means of speeding up process optimization [21–23] while at the same time maintaining industrially mandated tolerances for quantities such as roughness or hardness. The progress in high performance computing has made molecular dynamics (MD[1]) simulations and other meshless simulation methods a viable tool for studying the processes occurring during cutting or grinding [24,25], such as, e.g., chip formation and material removal [26] or surface topography evolution [27]. Notable previous efforts of simulating scratching, cutting, or polishing atomistically have usually been dedicated to understanding the removal of a single nanoscale chip from a monocrystalline flat surface [28,29] or from an isolated roughness feature [30,31] and to studying some of the occurring crystallographic processes [32,33]. Based on polycrystalline MD models featuring tens of millions of atoms, we can nowadays make predictions about the outcome of nanoscopic grinding and sliding processes that can be qualitatively translated to the micro scale because the simulated grains are sufficiently large to correctly reproduce a realistic material response [34,35]. Hence, MD simulations offer the possibility to understand the processes involved in grinding processes in terms of microstructural evolution and surface quality, thus being a powerful tool to optimize such processes.

If the need to model the machining process at the mesoscale outweighs the necessity to obtain in-depth crystallographic information to have a direct comparison to the real process, then there are related particle simulation methods available that can intrinsically handle the large deformations without the need to repeatedly re-mesh the model. Such methods include smooth particle hydrodynamics and the material point method (MPM), which have already been applied to model processes like scratching at ambient [36] and elevated temperatures [37] or micro-milling [38]. Such modeling approaches can be straightforwardly transferred to a grinding process [39] and have the additional benefit of being computationally much less expensive than MD.

Here we will demonstrate how to apply two related particle-based modeling methods to simulate, visualize, and analyze a grinding process at three different levels of detail. At our most detailed but also computationally most expensive level, MD simulations of a mild steel work piece are being developed to address microstructural aspects of realistic work pieces during grinding. Approximately seven times larger, a purely ferritic polycrystalline work piece, studied using large-scale MD, has the advantage that the grains can be constructed large enough so that the work piece qualitatively behaves like a macroscopic material. Thirdly, an MPM model at sub-mm scale dispenses with any explicit microstructure and replaces it with a continuum material model, but is of course more readily compared to real process conditions.

We will first give a detailed account of realistic MD microstructure generation for ferritic and mild carbon steel work pieces. Next, we will outline how to apply the MPM to model a grinding process at the mesoscale. We then give an overview of some of the available visualization techniques to study the chip formation as well as the surface quality, the microstructure, and the stresses in the work piece. An important aspect is the correct identification of the generated chips, which is necessary to properly track material removal and the topographic evolution. We conclude by applying our three modeling approaches to one exemplary case study per level of detail, discussing and interpreting the results from a process and a materials engineering point of view.

2. Models and simulation methods

All MD and MPM simulations were carried out with the open source software LAMMPS [40]. The three types of models employed in this work as well as an overview of the polycrystalline atomistic model generation are shown in Fig. 1.

2.1. Molecular dynamics (MD) simulations

The large-scale molecular dynamics models used for this work were constructed in Dream.3D [42], an open-source software designed for the 3D reconstruction of electron backscatter diffraction data and the production of synthetic microstructures from a set of statistics. Dream.3D operates on a voxel basis, i.e., the number of elements in the model influence only its spatial resolution, but not its absolute size. This constitutes a considerable increase in microstructural realism compared to other efforts based on a Voronoi construction [43]. Samples can be synthesized with periodic boundary conditions, but only either along all the Cartesian axes or none. As the atomistic export filter of Dream.3D was restricted to cubic lattices, a custom-made conversion interface was written in Matlab that would ultimately also allow the implementation of other lattices such as that of cementite.

We will give a brief account of the functionality of the self-written conversion interface. The HDF5 data structure of the Dream.3D output as shown in the top left of Fig. 1 can be accessed using Matlab's `h5read` function. The required data fields are all located in `/DataContainers/SyntheticVolumeDataContainer/CellData/` and are called `FeatureIds`, `Phases`, and `EulerAngles`. If a visualization in the style of an EBSD image is desired, importing the field `IPFColor` is also advantageous. In a first step, the spatial coordinates of all voxels associated with any given grain (whose grain number is stored in `FeatureIds`) have to be determined from their 3D indices scaled to the desired MD model volume. As numerous grains will be straddling periodic box boundaries, these grains must be "unfolded" to make them simply connected. This can be done by analyzing the histograms of the grain element coordinates along the three axes and moving all elements "below" the gap in the histogram in positive direction by one box length. Next, the Matlab function `alphaShape` was used to identify the region encompassing all grain elements, after which it must be ascertained that the number of identified regions per grain is really equal to one. The Euler angles of every grain, stored in the field `EulerAngles`, can then be converted to rotation matrices using the ZXZ' convention. After superimposing the desired lattice over the individual grain regions and rotating it by the corresponding rotation matrix, the Matlab command `inShape` was used to identify all atoms that lie within the alpha shape of the respective grain. Finally, the periodic boundary conditions must be reinforced so that all the grains extending beyond the simulation box are folded back into the box.

The resulting atomic system will exhibit several artifacts along the grain boundaries. Depending on the original number of elements used in Dream.3D, there may be vacuum gaps between neighboring grains caused by resolution limitations, and the purely mathematically constructed grain boundaries are not yet in thermodynamic equilibrium.

[1] **Abbreviations:** MD: Molecular Dynamics MPM: Material Point Method RMS: Root-Mean-Square

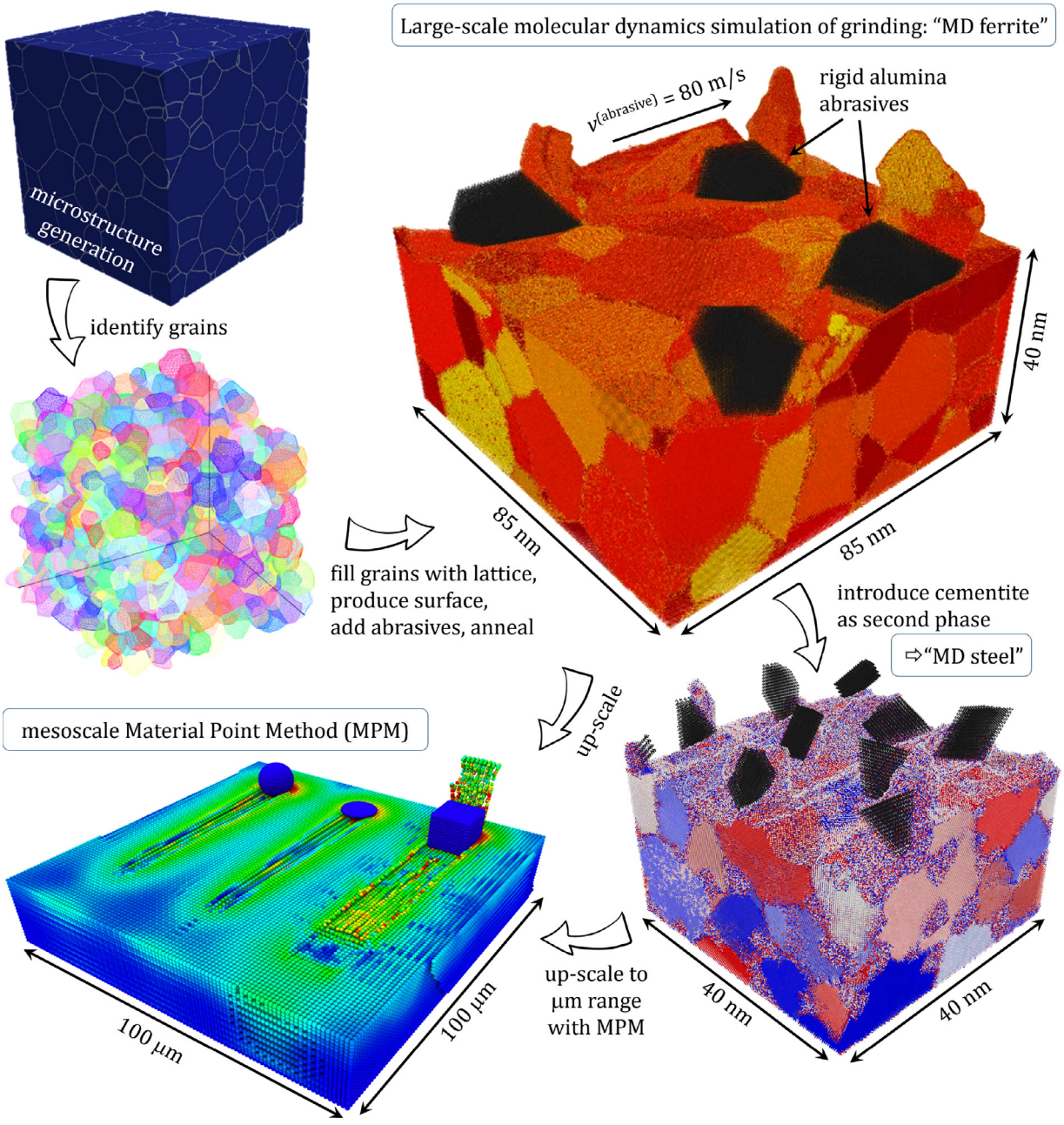

Fig. 1. MD work piece generation and system overview. The particle system visualizations were done in OVITO [41].

These issues can be resolved by proper heat treatment of the sample [44], but the subsequent loss of system volume should be accounted for during the construction, so this is likely to be a somewhat iterative process. Computational resources permitting, voxels corresponding roughly in size to a unit cell of the required lattice are desirable.

The primary MD model, a ferrite work piece with a bimodal grain size distribution, was constructed in Dream.3D as described above, cf. the top half of Fig. 1. This model will abbreviated as "MD ferrite" henceforth. Both grain sizes were chosen to be equiaxed, with mean grain diameters of 28.3 nm and 14.2 nm, respectively. The initial 3D-periodic system of $85 \times 85 \times 85$ nm^3 then holds approximately 200 grains that are randomly oriented. The initial Dream.3D microstructure was imported into Matlab, all grains filled with bcc lattices ($a = 2.86$ Å) oriented in the directions determined by Dream.3D, and then the free work piece surface was introduced at $z = 40$ nm. In the ferrite work piece, the Fe–Fe interactions are governed by a Finnis-Sinclair potential [45]. After energy minimization and heat treatment by heating up to 1100 K, followed by a cooling cycle down to 300 K, the grain boundaries were assumed to be in thermodynamic equilibrium.

As a simple model for a mild steel (abbreviated as "MD steel"), we introduced a cementite (Fe_3C) phase, see the bottom right panel in Fig. 1. This secondary MD model was built in a similar way as the ferrite, except that the smaller grains were filled with a cementite lattice as a second phase. Cementite is an orthorhombic crystal with lattice constants $a = 4.514$ Å, $b = 5.08$ Å, $c = 6.734$ Å. It is a hard and brittle ceramic that is present in steels up to a carbon content of 2.06wt%. For the steel substrate, we used a three-body Tersoff interaction potential with the parameters taken from [46]. This potential has been thoroughly tested [47] and considered suitable to study combinations of the ferrite and cementite phases as required to properly represent our simple steel work piece. This particular microstructure contains 6.45at% of carbon, which corresponds to 1.7wt%. However, the increased realism of

being able to model steel comes at a considerable computational cost: depending on how well they are optimized, the simulations run 4–11 times longer than for the MD ferrite system. This explains why for this preliminary study we had to settle for a steel work piece measuring only $40 \times 40 \times 25$ nm^3 in order to obtain results within reasonable times (several days per simulation run), thus also reducing the mean grain sizes to 12.7 nm for the ferrite phase and 5 nm for the cementite phase.

The abrasives representing the grinding tool were constructed as alumina (α-Al_2O_3), which crystallizes trigonally with lattice constants $a = 4.75$ Å and $c = 12.98$ Å. The oxygen atoms form layers with hexagonal densest packing with the aluminum atoms on six-membered rings between them. Alumina parallelepipeds with Gaussian size distribution were prepared and placed with varying rake angles above the work piece surface as can be seen on the right side of Fig. 1, following a protocol that is described for generic abrasives in Ref. [43]. The large, ferritic work piece was fitted with two different abrasive sizes and distributions: 13 abrasives with a mean diameter of 20 nm (not shown) and 3 abrasives with a mean diameter of 45 nm. In the case of the smaller abrasives, a projection of the abrasives onto the work piece surface yields an areal fraction of 17%, whereas for the three larger abrasives, we get an areal fraction of 22%. The steel work piece was ground by a distribution of 8 abrasives with a mean diameter of 13 nm, leading to a projected areal fraction of 20%. In contrast to some other recent modeling efforts [29], due to our large work piece size we have made the computational simplification of assuming the grinding tool to be completely rigid. It interacts with the work piece via a Lennard-Jones (LJ) potential, with $\sigma = 2.203$ Å, $\varepsilon = 0.095$ eV, and a cutoff radius of 10 Å.

During the grinding simulations, periodic boundary conditions were applied in both lateral directions. A constant normal pressure between 0.1 and 0.9 GPa was applied to the abrasives in $-z$ direction. Simultaneously, the abrasives were moved at constant speed of $v_x = 80$ m/s and $v_y = 9$ m/s over the work piece, cutting chips of various lengths and shapes depending on the applied pressure and the simulation time. The velocity component in y direction was introduced to prevent the abrasives from immediately grinding in their own grind marks upon re-entering the periodic simulation box from the $-x$ direction, but rather meet up with the same portions of the work piece after approximately 10 passes. Thus, these kinematics correspond well to RPM-Synchronous Grinding processes [48,49], where the same abrasives come into contact with the same work piece areas again and again in the course of machining, which means that the work piece surface can be influenced in a much more defined way than with comparable conventional grinding processes. The time step was set to 2 fs, and a Langevin thermostat with a coupling time of 3.5 ps was applied in y direction to keep the temperature of the substrate at the desired value while reproducing a realistic heat conductivity of ferrous work pieces [44]. The lowest 3 Å of the work piece were kept rigid to avoid torque on the work piece during grinding.

2.2. Mesoscopic MPM approach for steel

The MPM is a continuum mechanics method and differs as such in many respects from conventional molecular dynamics approaches. Common to both approaches is only the time evolution of the system by solving the Verlet equations for each interaction center, which however are space filling, deformable volume elements, so called particles, of chosen size (resolution) in MPM rather than atoms like in classical MD. By smearing out the atomistic degrees of freedom the method can encompass much larger scales, thus samples in the cm range with simulation times of up to seconds can be studied within feasible time. This makes a direct comparison with experiments possible. By loosing the atomistic information and treating the material as a continuum, however the microstructure in the substrate cannot be resolved anymore. The material properties are described in an volume averaged manner by using uniform material parameters for the whole substrate such as Young's modulus, heat capacity, thermal conductivity, yield stresses etc.

Table 1
Johnson-Cook parameters for AISI 4340 steel [51]. Here, $\dot{\epsilon}_0$ is the equivalent plastic strain rate and σ_Y the material yield stress at zero strain. B and n are strain hardening parameters, C a strain rate parameter, m a temperature coefficient, and T_m the melting temperature.

σ_Y (MPa)	B (MPa)	C	n	m	$\dot{\epsilon}_0$ (1/s)	T_0 (K)	T_m (K)
792	510	0.014	0.26	1.03	1.0	294	1520

The equations of motion in continuum mechanics are given by the Euler equations conserving energy, momentum and impulse of the system

$$\frac{\partial \boldsymbol{v}}{t} = \frac{1}{\rho}\nabla \cdot \boldsymbol{\sigma} + \boldsymbol{b} \tag{1}$$

$$\frac{\partial \rho}{t} = -\nabla \cdot (\rho \boldsymbol{v}) \tag{2}$$

$$\frac{\partial q}{t} = \kappa \nabla^2 q - \nabla \cdot (q\boldsymbol{v}) + W_p(t). \tag{3}$$

Eqs. (1) and (2) describe the mechanical flow, where $\boldsymbol{v}$ is the velocity, ρ the mass density, $\boldsymbol{b}$ a vector of body forces or imposed boundary forces and $\boldsymbol{\sigma}$ the Cauchy stress tensor. The temperature field evolves in time according to the advection-diffusion equation, Eq. (3), where q is the heat and κ is the thermal conductivity coefficient, and also according to heating due to plastic deformation, $W_p(t)$.

To solve the spacial partial differential equations they are mapped onto a set of simple algebraic equations for each volume element (which caries then the physical properties like stresses/strains, velocities, masses etc. at their respective location in the substrate) by use of a discrete set of basis functions and an auxiliary grid which is discarded after every simulation step. A detailed description of the MPM and the discretization used therein can be found in [38].

In order to remain close to an industrially relevant setup, several decisions regarding the most relevant factors were made. Given the parameters above, a Ni-Cr-steel alloy with a low carbon content of 0.32–0.44wt%, characterized by high strength and low fatigue, was chosen as ideal for the MPM simulations. This AISI 4340 steel is preferentially used in gear boxes and other mechanical devices exposed to high risk of wear, thus making it a universally recognizable choice for many applications.

Together with the solution of Eqs. (1) and (2), a material model is necessary that captures the correct response of the material in terms of stresses when it experiences deformations. This material model plays a similar role here as the empirical interaction potential used in classical MD. For steel, and in general for ductile materials, the Johnson Cook model [50] is well established, with the parameters for AISI steel used in this work listed in Table 1.

The exemplary steel block shown in the bottom left corner of Fig. 1 has a size of $100 \times 100 \times 20$ m in x, y, and z, with three generic types of abrasives (cone, sphere, cube) grinding across the surface in parallel at identical infeed depths to demonstrate different modes of chip formation.

To systematically study the influence of the abrasive grain orientation and infeed depth of a cubic abrasive on the grinding process, simulation runs on a steel surface of $200 \times 30 \times 20$ m in x, y, and z were carried out with a single cubic abrasive, where the work piece elements were placed on a simple cubic grid with a lattice constant of 1 m. The cubic abrasive with a side length of 10 m was constructed using COMSOL 5.2a by placing a trigonal mesh with maximum mesh size corresponding to the work piece lattice on its surface. In LAMMPS, these mesh points are finally mapped onto explicit particles, and the resulting abrasives are assumed to be rigid and isothermal. While this choice of abrasive shape is somewhat simple, it does offer the benefit of being able to efficiently study the material removal behavior of sharp-edged abrasives, which is strongly orientation dependent. The exact same shape

of abrasive has already been used in earlier work [52] to successfully prove that empirical macroscopic wear laws hold at nanoscale as long as the contact is not of a single-asperity nature. A more realistic abrasive shape would have had the disadvantage of requiring the study of a large number of orientations in order to extract meaningful information. When simplifying a grinding process to the interaction of one abrasive with the work piece surface, one has to be aware that the choice of abrasive grain size and simulated work piece width, or rather the ratio between the two, represents a particular fraction of abrasives in the grinding tool. In our system, this ratio was set to 1/3. The cubic abrasive was first oriented with one of its edges pointing towards the work piece and oriented parallel to the grinding direction ("edge"), then with one of its faces parallel to the work piece surface and one face facing in grinding direction ("flat"), and finally with one of its faces parallel to the work piece surface and an edge pointing in grinding direction ("ship").

The abrasives were first indented into the work piece to the appointed infeed depths of 3, 5, or 7.5 m by setting the total force on the grinding tool to zero, and then they were moved at constant infeed depth and a constant velocity of $v_x = 10$ m/s. The lowest layer of the substrate was kept fixed to avoid that the material block starts moving. Non-periodic boundary conditions were applied. The time step in the MPM simulations is not constant over the simulation run, i.e., it varies depending on the current shear stiffness G, density ρ, and bulk modulus K. In general one can say the harder the material the smaller the time step. In the current simulation it was in the range of 100 ps.

The temperature T_0 of the system was set to 294 K. Heat was produced during grinding by the conversion of energy from the plastic deformation. Heat transfer between the particles of the substrate was enabled by applying a heat conductivity coefficient $\kappa = 44$ W/(mK) for unalloyed steel. The reference density ρ was set to 7830 kg/m and the Young's modulus to 207 GPa.

3. Results and discussion

To show the capabilities and advantages of our meshless simulations of grinding, we will now present our results obtained for the three different levels of detail. While the MD ferrite system offers the microstructurally more accurate description of the work piece response [53], it does not contain any hard carbide phases and is therefore a simplified version of a ferritic work piece. This issue is addressed in the second MD system featuring a two-phase mild carbon steel, sacrificing system size for computational manageability, which leads to a fully realistic nanocrystalline work piece. Our last example does away with any explicit microstructure altogether and can therefore not resolve any grain-specific phenomena, but is able to reproduce a macroscopic grinding process and can be more readily compared to experimental results [54].

3.1. Molecular dynamics simulation

Fig. 2 shows an overview of several modes of data representation to visualize and evaluate the work piece and the chips during the grinding process. The work piece is sliced into tomographic sections to investigate the time development of key aspects and quantities: from top left to bottom right in Fig. 2, the colors of the atoms correspond to the grain boundary structure and identified chips, the atomic flow velocities, the crystallographic grain orientations, and the stresses in grinding direction. The off-diagonal elements are representations obtained by eliminating, e.g., lateral resolution of the work piece to produce depth- and time-resolved maps of the grain boundary fraction (top right) or the stresses in grinding direction (bottom). The bottom left panel shows a representative topographic view of the work piece surface without the matter that has been identified as chips. The above visualization techniques are described in more detail elsewhere [10,55], but in the next two paragraphs we will describe in depth our approach to proper chip identification.

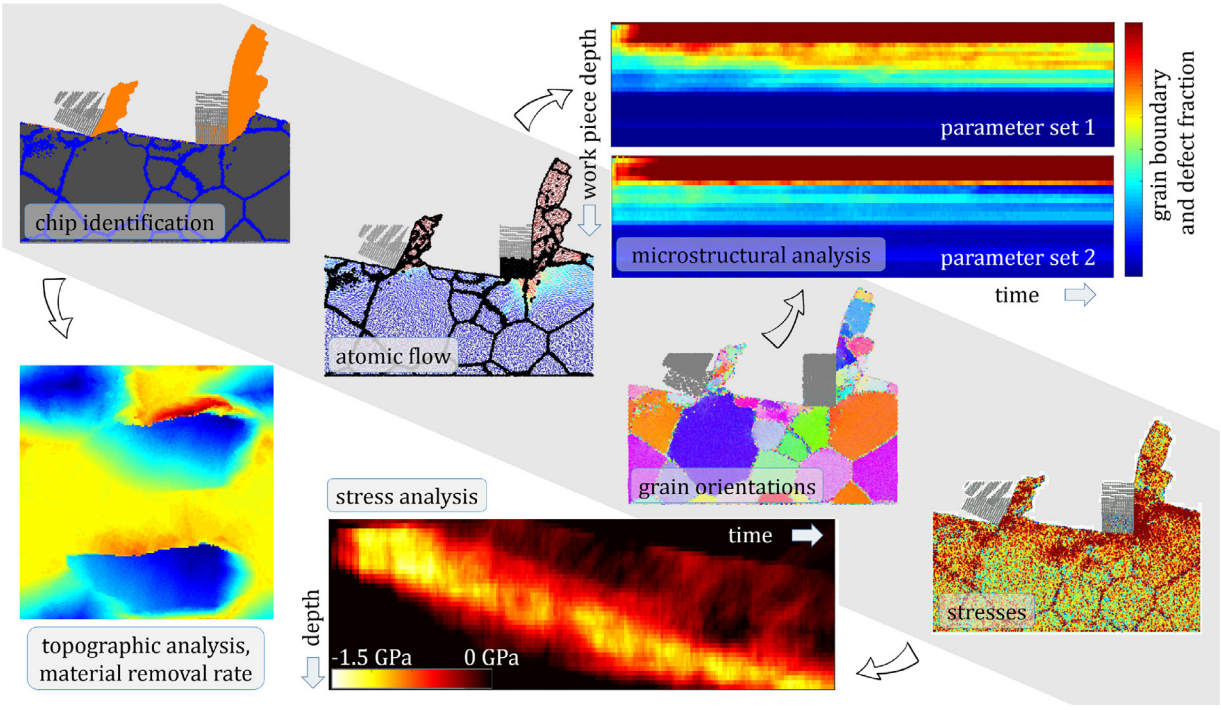

Fig. 2. Visualization and analysis workflow. Diagonally from top left to bottom right, visualizations are based on a common neighbor analysis [56] combined with our chip identification algorithm described in the main text, a vector plot of atomic flow velocities (after filtering out thermal fluctuations), electron backscatter diffraction imaging of the grain orientations, as well as the stresses in grinding direction within the work piece (compressive stresses are red). The bottom left shows a typical topographic visualization of the work piece surface during grinding. The depth-resolved maps track the time development of laterally averaged key quantities such as the grain boundary and defect fraction (top right) or the stresses (center bottom). (For interpretation of the references to color in this figure legend, the reader is referred to the web version of this article.)

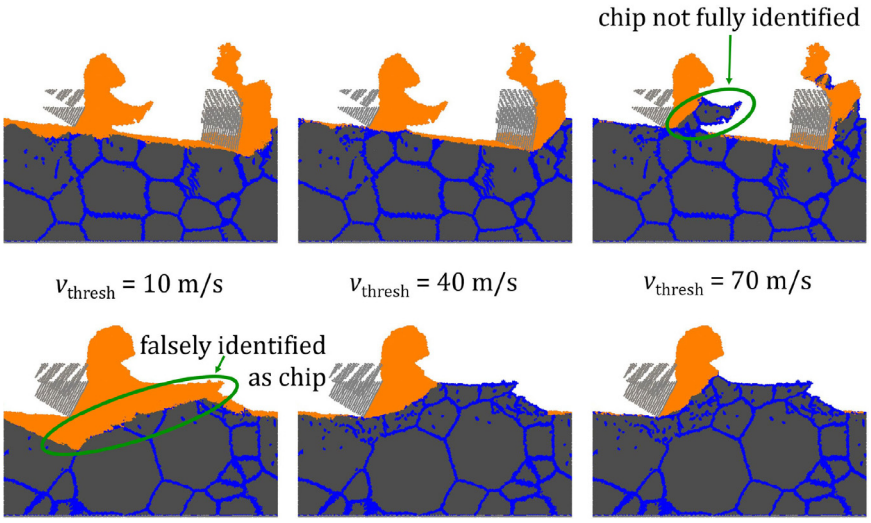

Fig. 3. Chip identification: comparison of three different threshold velocities v_{thresh} determining which atoms are identified as a chip in two representative tomographs. Chip atoms are orange, bcc atoms gray, grain boundaries blue. Once an atom has been identified as part of a chip, it remains so until the end of the simulation. The green ellipses at v_{thresh} = 10 m/s and v_{thresh} = 70 m/s mark problematic regions that are falsely identified as either chip or work piece due to the non-ideal choice of the threshold velocity. (For interpretation of the references to color in this figure legend, the reader is referred to the web version of this article.)

In MD simulations, matter usually does not leave the system. Furthermore, as surface passivation is not accounted for, machined work pieces may act more ductile, especially at the direct interface between work piece and a forming chip [54]. Brittle fracture, separating chip from work piece at an obvious location, is typically not observed for these types of material, as opposed to others [57]. To be able to estimate the material removal rate and to get a reasonable image of the resulting topography, it is therefore important to identify the formed chips in an automatized way. Previous approaches to this problem used the momentary advection velocity of the work piece atoms to determine whether they were part of a chip or still part of the work piece [27]. There, a fraction of the grinding speed was defined as a threshold velocity above which an atom was considered part of a chip. These approaches work well for comparatively spherical abrasives that plow more than they cut, thus not producing longer chips. However, in our current systems, the sharp edges and the rake angles of the alumina abrasives can lead to the formation of long chips. The problem with such chips is that they may start swaying due to inertial forces, leading to variations in their velocity relative to the work piece, which means that they may or may not fulfill the criterion for being recognized as a chip depending on how they sway. This causes small to medium artifacts in the amount of removed matter, but the main drawback here is that all matter that is not recognized as a chip is automatically considered part of the work piece, which in such a case leads to temporary "work piece exclaves" that may be far from the actual surface, making a visualization of the time-dependent surface topography or a calculation of roughness parameters virtually impossible.

As chip formation is a cumulative process, one could reasonably define that any atom that has ever moved in grinding direction at a velocity higher than a certain threshold velocity v_{thresh} becomes and remains part of a chip, even if its advection velocity should ever drop below this threshold. The threshold velocity v_{thresh} must then be fine-tuned to minimize artifacts of failed chip identification versus false chip identification, see Fig. 3. Here, marked by green ellipses, it can be seen in the left column that v_{thresh} = 10 m/s, corresponding to 1/8 of the grinding speed, leads to large parts of the work piece being identified as a chip, while in the right column we see that v_{thresh} = 70 m/s fails to identify obvious portions of chips. The former can be attributed to the fact that even those parts of the work piece surface that are effectively only being plowed aside during the grinding process and definitely remain part of the work piece can temporarily exceed an advection velocity of 1/8 of the sliding velocity. The "failure" to identify considerable portions of the chip for the high threshold velocity is probably more a problem of delayed identification, but this leads to disruptive artifacts especially in the time development of the work piece topography, as even small unidentified chip portions disjunct from the actual surface have a large impact on the roughness parameters. Put simply, reducing v_{thresh} pushes the transition between work piece and identified chip further into the work piece, so the task is to find a stable value for this parameter that is globally applicable to all our systems. We found that defining v_{thresh} = 40 m/s, corresponding to half the grinding speed (see the central column in Fig. 3), produced the best overall reproduction of what a human observer would have considered work piece and chip. The thin layer of chip material that may redeposit on the work piece surface because it was accelerated to just above the threshold velocity by a passing abrasive but in fact never became part of a chip (e.g., in the upper middle panel) constitutes only a small offset to both the removed matter tally as well as the surface topography.

Having found an adequate threshold velocity for chip identification, we can now correctly analyze the removed matter and the surface roughness. As the abrasive grain size significantly affects the surface quality of the machined work piece, we investigated the amount of removed matter and the RMS surface roughness for two different mean abrasive grain sizes (13 abrasives with d = 20 nm and 3 abrasives with d = 45 nm). In Fig. 4 we show the amount of matter removed from the ferrite work piece and the RMS surface roughness S_q (equivalent to the standard deviation of the topographic heights) over the grinding distance, as well as the mean material removal rate over the normal pressure for both investigated abrasive grain sizes.

In general, material removal progresses linearly for both abrasive grain sizes because the grinding processes were carried out in a load-controlled fashion so that the abrasives move further and further into the work piece as more matter is removed, see the top left panel in Fig. 4. This allows us to define the material removal rate as the slope of these straight lines, giving us the mean removed matter depth per grinding distance, which is a non-dimensional parameter that lends itself to cross-scale comparison, see the bottom panel in Fig. 4. From this graph we can see that increasing the abrasive grain size by a factor of about two leads to an increase in the material removal rate by a factor of more than 5 depending on the normal pressure. This can be explained primarily by the number of abrasives per unit area, which decreases with the square of the abrasive diameter [58]. However, due to the sharpness of the abrasive tips, the contact area of each abrasive does not increase with the square of its diameter, leading to an overall reduced contact area for the larger abrasives. Thus, the larger abrasives penetrate deeper into the work piece at equal normal pressures, leading

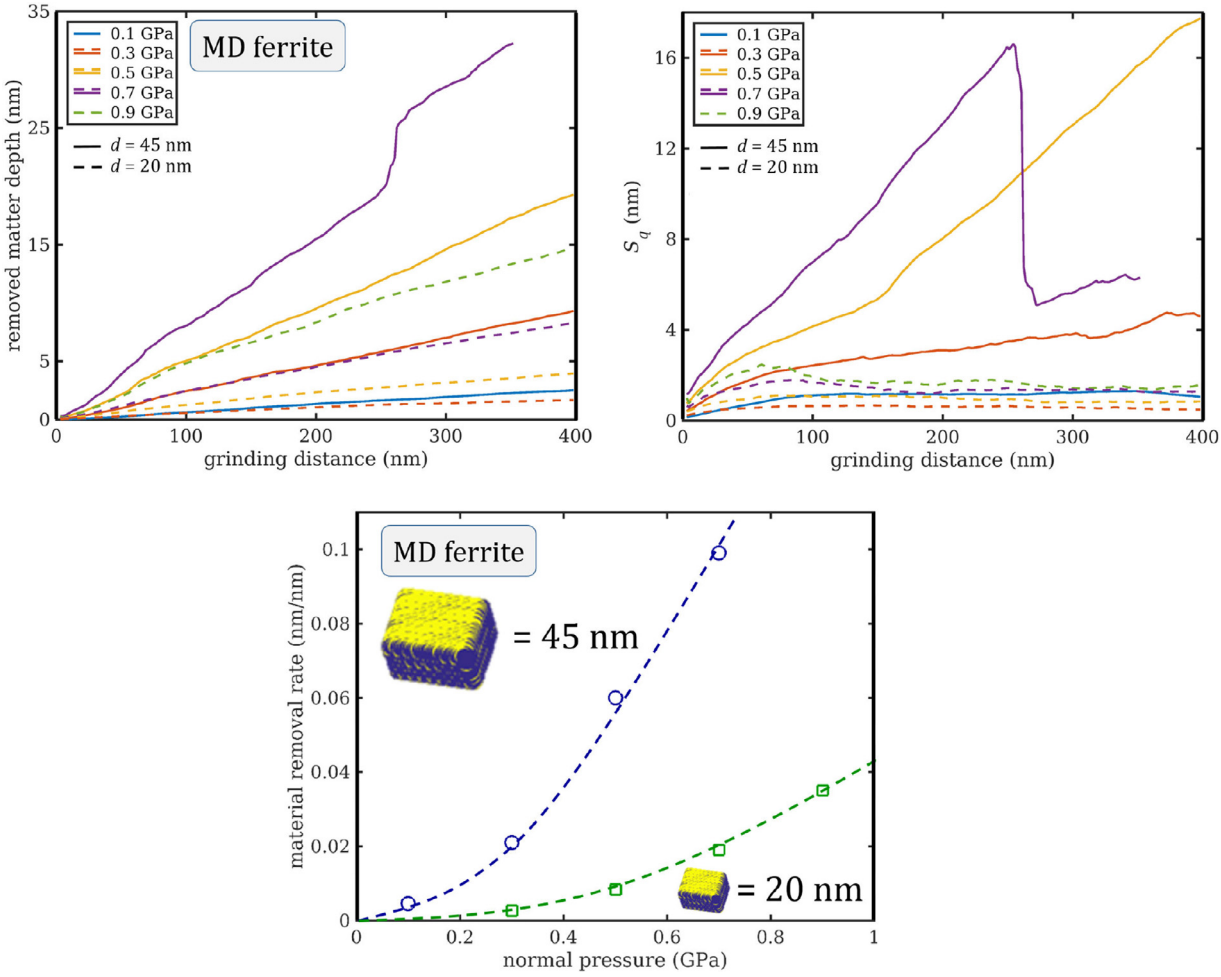

Fig. 4. Top: Removed matter depth and RMS roughness S_q as a function of grinding distance for two different abrasive sizes (diameter d) grinding the ferrite work piece. Bottom: the mean material removal rate in units of nm removed matter depth per nm of grinding distance as a function of normal pressure for two different abrasive sizes.

to cleaner chip formation and better material removal. Also, due to a decrease in the total number of cutting edges, the chance of an abrasive following immediately in the track of another, and therefore hardly removing any matter, is reduced with increasing abrasive size [8]. Finally, it has to be kept in mind that the areal fraction of the large abrasives is approximately 30% higher than that of the small abrasives. As the potential material removal increases, the ground surface quality deteriorates due to a concurrent rise in the equivalent chip thickness, because the height differences and the lateral distances between machined and unmachined portions of the work piece are larger. Thus, in the selection of grinding parameters, a comparison of the grain sizes is typically carried out balancing the material removal rate with the mandated surface quality. Therefore, each grain size is assigned a specific working range: fine grains are used for fine grinding and coarse grains for rough grinding [8].

As mentioned before, the higher efficiency achieved by increasing the normal load or the abrasive grain size comes at the price of lower surface quality, i.e., higher surface roughness, see the time development of S_q in the top right panel. For the 20 nm abrasive grains one can see the initial increase of S_q to a maximum value with a subsequent decrease and a saturation to some optimum value that depends on the abrasive grain size and the normal pressure. Thus, for the lower abrasive grain size, an increase in normal pressure significantly increases the efficiency while only marginally decreasing the surface quality. By contrast, the surface roughness increases by a much higher amount with higher normal pressure when grinding with larger abrasive particles. However, the time until saturation of the surface roughness also depends on the abrasive grain size and the lateral distribution of the grains, so that for the three 45 nm grains, we can only observe the maximum S_q value for the lowest normal pressure of 0.1 GPa after our total grinding distance of 400 nm. This may give the impression that S_q would keep on rising indefinitely (as the solid yellow curve for 0.5 GPa may suggest), but it is merely a restriction of the system size combined with a load-controlled grinding process.

Note that grinding at 0.3 GPa with 45 nm abrasives and grinding at 0.7 GPa with 20 nm abrasives incidentally produces almost exactly the same material removal rate of 0.02 nm/nm, while the S_q varies by a factor of ≃2. We will use this similarity as a basis for comparison, focusing on aspects that can only be elucidated using atomistic simulations such as microstructural ones. The lateral spacing between the 45 nm abrasives perpendicular to the grinding direction (see the top right panel in Fig. 1) leads to a horizontal ridge being formed, manifested by the strongly rising S_q parameter for this abrasive size at medium and high normal pressures. The quality of such a ridge can be seen for 0.3 GPa in a topography image shown later in this work. The purple curves representing the large abrasives at the highest normal pressure of 0.7 GPa in the top row of Fig. 4 exhibit noteworthy behavior after approximately 250 nm of grinding. After a grinding distance of 250 nm, two abrasives in close proximity quickly grind away the entire horizontal ridge, which causes a noticeable increase in the removed matter thickness and a sudden drop in the overall RMS roughness from 17 nm to 5 nm. It should be noted that after this drop, the saturation surface roughness has not been

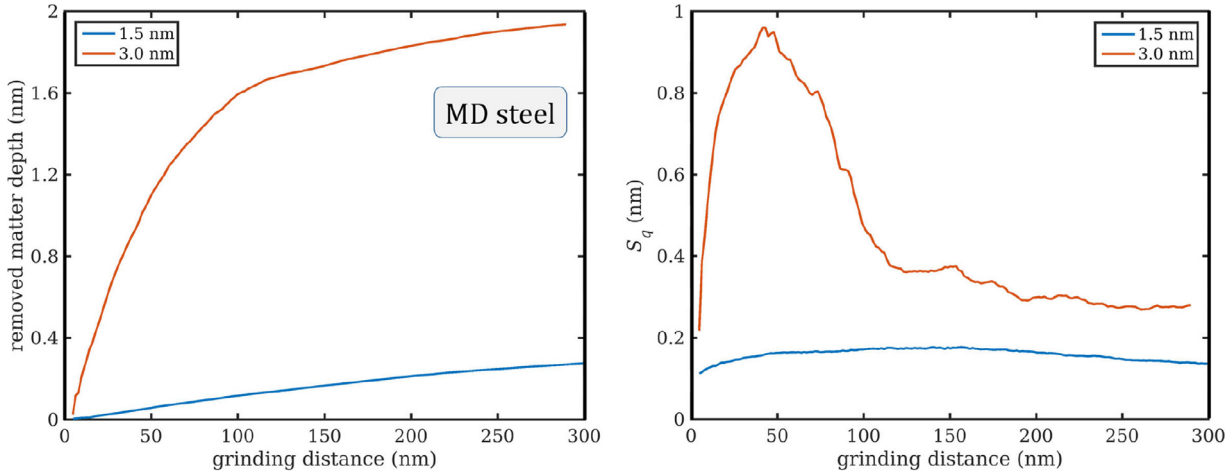

Fig. 5. Removed matter depth and RMS roughness S_q for the small steel work piece. Note that the steel simulations were run at constant infeed depth, not at constant load.

reached, but the surface roughness continues to increase. Such behavior may be considered an artifact of this combination of process parameters, located at the boundary of the parameter space (high pressure, few abrasives, load-controlled grinding) that can be reliably represented using large-scale MD simulations.

In Fig. 5, the amount of removed matter and RMS surface roughness S_q on the small steel system with 13 nm abrasives is shown as a function of grinding distance. One relevant difference to the MD ferrite system with respect to process conditions is that the abrasives are moved at constant infeed depth here, not under constant load. This is clearly recognizable for 3 nm infeed depth in the saturation of the removed matter depth curve to a constant amount after around 100 nm of grinding distance, because the abrasives have covered most of the work piece by that time, but cannot indent any deeper to remove more matter. The non-linearity of the removed matter depth in this infeed depth controlled process somewhat limits the comparability to the material removal rate data shown in the bottom panel of Fig. 4. However, the initial slope amounts to approximately 0.02 nm/nm, which lies well within the range of what was observed for the larger MD system. It seems that for the smaller infeed depth of 1.5 nm, the grinding distance of 300 nm is not sufficient for saturation of the removed matter depth in particular. Despite this, the surface roughness seems to have saturated already resulting in a quite low surface roughness of about 0.1 nm. At infeed depth 3 nm, however, it is clear that the maximum roughness of the work piece is overcome after approximately 120 nm of grinding, and that grinding any further does not significantly improve the surface quality any more, which is typical of an infeed depth controlled process. Note that since we start all our simulations with an atomically flat work piece, the lowest achievable surface roughness will always end up higher than in the beginning, depending on the abrasive size and the infeed depth.

While studying the time-development of a roughness parameter like S_q, as shown in Figs. 4 and 5, is instructive, it may also be misleading, as the entire surface topography is represented only by one scalar value. Therefore, production and quality engineers will usually also insist on viewing representative surface images to obtain a better feeling for the quality of a ground surface that may not be well represented by a set of parameters alone. The topographies of two comparable ferrite and one steel work pieces are shown in Fig. 6 after a grinding distance of 240 and 112 nm, respectively. The value for MD steel was chosen to correspond to that of MD ferrite in terms of relative grinding progress, as its lateral dimension is only 47% of the larger system. For the two representative MD ferrite systems, the same material removal rate was obtained for grain sizes of 45 and 20 nm and normal pressures of 0.3 and 0.7 GPa, respectively. However, the surface with the smaller abrasives looks much smoother than the one using only three big abrasives (note the difference in color scaling for the left and center panels in Fig. 6), which is also reflected in the time development of the S_q parameter of the two systems shown in the top right panel of Fig. 4. In the panel on the right the surface of the steel system is displayed. Since this surface is ground at constant infeed depth, it is already smoothed after approximately 30% of simulation time and does not improve significantly until the end of the grinding process, cf. Fig. 5 (right panel).

The chip formation and microstructure are shown for a representative tomograph under four different sets of grinding parameters in Fig. 7. As it is to be expected, the chip formation varies strongly between the different settings, ranging from a very short drizzle to a continuous string of metal forming in the contact area. This is especially interesting to compare for identical material removal rates, but different grinding conditions. At 0.7 GPa with an abrasive grain size of 20 nm, the average material removed over time will be very much the same as with 0.3 GPa and abrasive grain size of 45 nm, but the shape of the formed chip is completely different. Obviously, with a smaller abrasive grain and higher pressure, the impact on the work piece will have a different effect on the structure below. This effect on the resulting defects of the work piece will be made visible in Fig. 8. Additionally, the larger chip created by the larger abrasive grain will remove more heat from the contact zone in a shorter amount of time and will also feature a different ratio of deformations, such as compacting and plowing, which is also observed in real-life cutting and grinding processes [2]. Naturally, this will have a major impact on the resulting microstructure development underneath the contact zone, as heat and deformation are the two main driving forces for microstructural changes [10]. Depending on the degree of microstructure development and thus also the mechanical properties, this might significantly affect the material response to ongoing mechanical loading. In a recent study about the microstructural development in nanocrystalline ferrite during grinding, it was shown that mechanical loading leads to grain growth by grain boundary migration and lattice rotation in the near-surface zones [10]. With increasing load, not only the chip volume increased, but also the microstructural modifications advanced further into the material. Similar microstructural trends can be expected and are observed here (top row in Fig. 7), even though grain refinement will be more dominant here as the initial grain size is roughly two times larger in the present system. This lower heat input and varying deformation ratio is an additional reason why, in most cases, an efficient machining setup uses the largest available cutting edge that is able to produce an acceptable surface quality. The optimum cutting edge size depends on the exact operational parameters involved, like rotational or counter-rotational synchronicity, or the general grind-

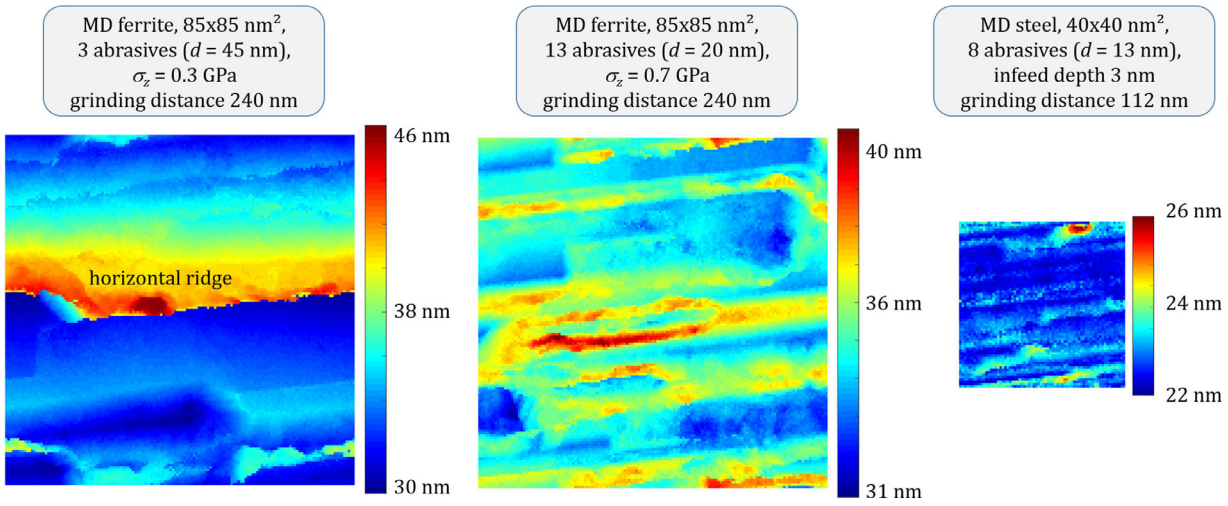

Fig. 6. Qualitative topography comparison between two different abrasive grain sizes grinding on ferrite at the same material removal rate and the same total removed matter depth. Note that at this grinding distance, the grinding tool with the three abrasives has not yet covered the entire work piece surface, with the portion not yet machined forming a horizontal ridge. The topography of the smaller steel work piece is shown on the right after equivalent linear grinding progress (shorter grinding distance — constant infeed instead of constant normal pressure).

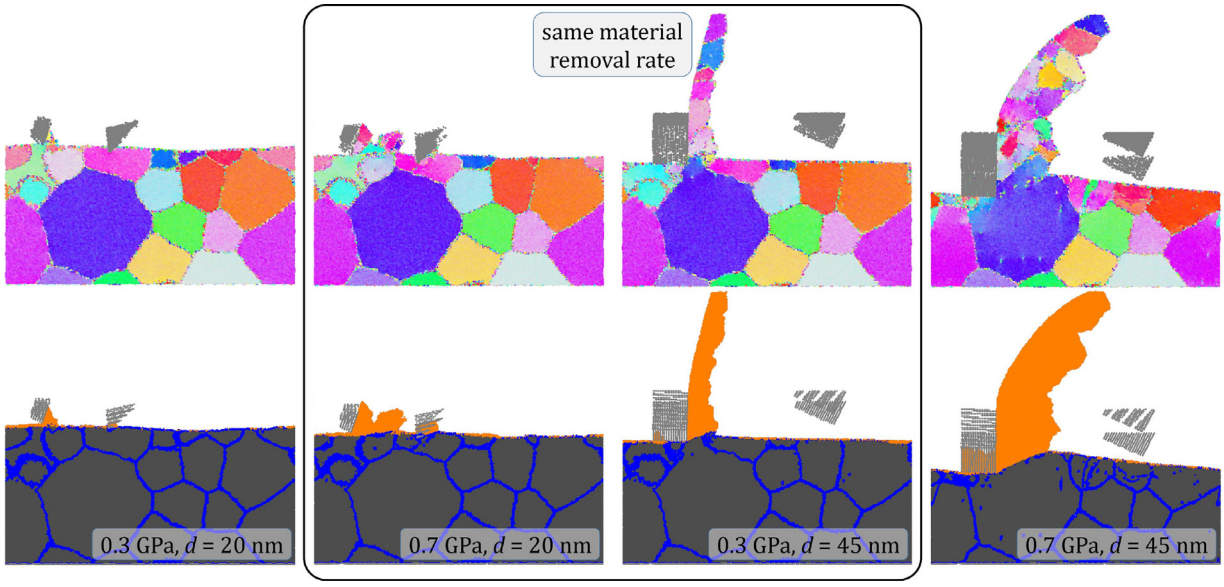

Fig. 7. Chip formation and microstructure evolution of ferrite after 1 ns of grinding. The slices are arranged from left to right with increasing severity of the grinding conditions, see legend, where d is the mean diameter of the abrasive particles. Note that the central two examples feature the same average material removal rate.

ing process [5,9]. Here again, all the relevant characteristics of the work piece material and grain type, as well as many impact parameters come to bear. Of all the impact parameters, the attack vector of the grain as well as the rotation and direction of the grain's edges and points are especially important [8], an effect that will be explored further on in more detail. All involved parameters, among which temperature and pressure play an important role, influence the structure of the work piece. The resulting effects are clearly visible in both Fig. 7 and Fig. 8 in form of micro cracks and shear stresses [59]. All in all, the simulation presented here produces a realistic chip shape and size [2,54], factored down by several orders of magnitude and without the scaling problems previous simulation efforts encountered in the past [53]. Though the results are remarkable, the range of length scales the simulations cover is too small to show the full impact of the deformations caused by the grinding process, which will be complemented by the mesoscopic MPM simulations further on. However, the atomistic simulations can show additional effects that are usually inaccessible to standard quality control procedures such as light microscopy or profilometry, so they open up exciting potential for process optimization.

As described above, the stresses introduced into the work piece and the resulting microstructural changes have a major impact on the mechanical behavior and thus on the material response to mechanical loading. Therefore, in Fig. 8, we present a comparison of the depth-resolved time-development of the stresses and the microstructure in the work piece. It is known that the removal of larger chips introduces less stress into the work piece [53]. To visualize this impact, we compare two grinding processes with different abrasive grain sizes that feature almost identical material removal rates (see also Fig. 4). The central maps (in jet-style coloring) show the time development of the grain boundary and defect fraction as a function of the work piece depth. The saturated red areas mark regions where the matter has already been removed, and in the bottom two panels we have traced the evolving work piece surface as dash-dotted lines to guide the eye. Dark blue regions represent the grain size and defect density of the microstructurally unaltered

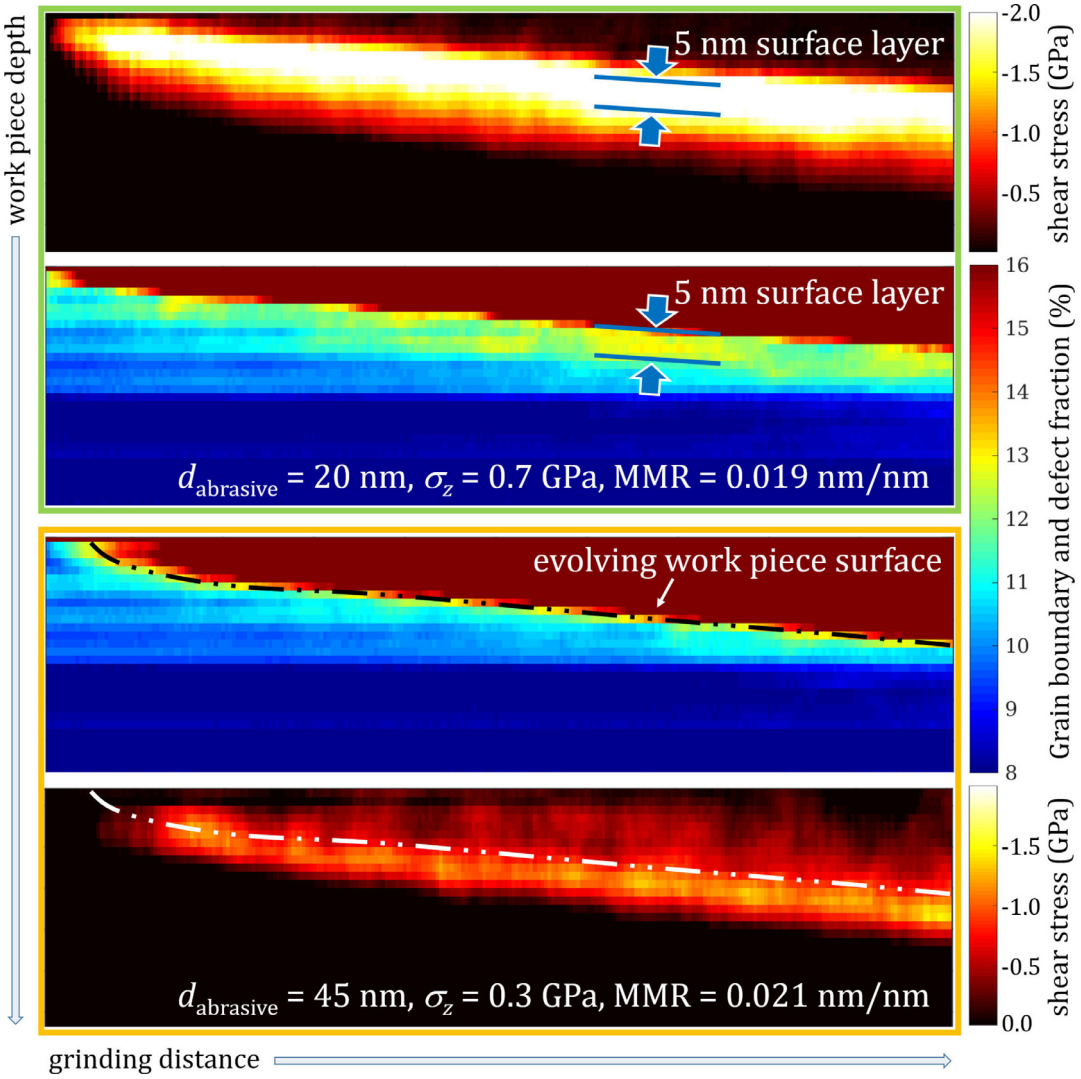

Fig. 8. Comparison of the microstructural development (central maps) and the shear stress profile (outer maps) in the work piece for two different parameter combinations that led to the same material removal rate. Top system (green frame): $d_{abrasive}$ = 20 nm ("small"), σ_z = 0.7 GPa ("high"); bottom system (orange frame): $d_{abrasive}$ = 45 nm ("large"), σ_z = 0.3 GPa ("moderate"). (For interpretation of the references to color in this figure legend, the reader is referred to the web version of this article.)

work piece. The higher normal pressure required to achieve the same material removal rate with smaller abrasives leads to a surface layer (between the two parallel lines) of increased grain boundary and defect density that may indicate grain refinement and hardening [32]. Defects in the form of dislocations are generated to release stored elastic energy at the very beginning of grinding directly below the tips of the indenting abrasive particles, as has been shown in a MD nanoindentation study of copper by Li *et al.* [32]. Upon further indentation and with growing load and stress the dislocations are moving further away from the work piece surface, while partial dislocations are also emitted from GB triple junctions [32]. The central maps are bracketed from the top and the bottom by the corresponding maps of the stresses in grinding direction within the work piece (in fire-style coloring). Note that the color ranges are identical for both maps. When the abrasives start moving across the surface, the stresses and the defect density will first increase as a result of higher forces and temperatures before saturating to a stable level [33]. Looking at the typical stresses in the work piece, it can be seen that the more highly loaded case with the smaller abrasives also leads to lateral stresses roughly double those in the lower-load case (−1 *vs.* −2 GPa). When comparing the upper two panels, it seems that the microstructurally modified surface layer develops in the region where the stress in grinding direction exceeds −2 GPa in the negative direction and the respective stress map saturates to white. This is quite reasonable considering that the sub-surface stresses are the driving force for defect formation such as dislocation emission and lattice rotation [10,32,33]. Considering the lower normal pressures that are necessary to achieve the same material removal rate for the larger abrasives, there are lower stresses developing in the near-surface zones and in second consequence a lower GB and defect fraction. Additionally, the higher average indentation depth of the abrasives leads to cleaner cutting of the chip rather than plowing which also aids to generate less defects. This analysis approach presents a good visualization method of near-surface effects and helps predict the impact of varying a given set of machining parameters. A full correlation of the effects observed in our simulations with those seen in real grinding processes requires a cooperated effort between simulation and hands-on data from real applications. This is work in progress and will be presented in a follow-up study.

3.2. Mesoscopic MPM simulations

The 3D simulation snapshots in Fig. 9 give a general overview whether a chip is formed during grinding or not, and also which size and

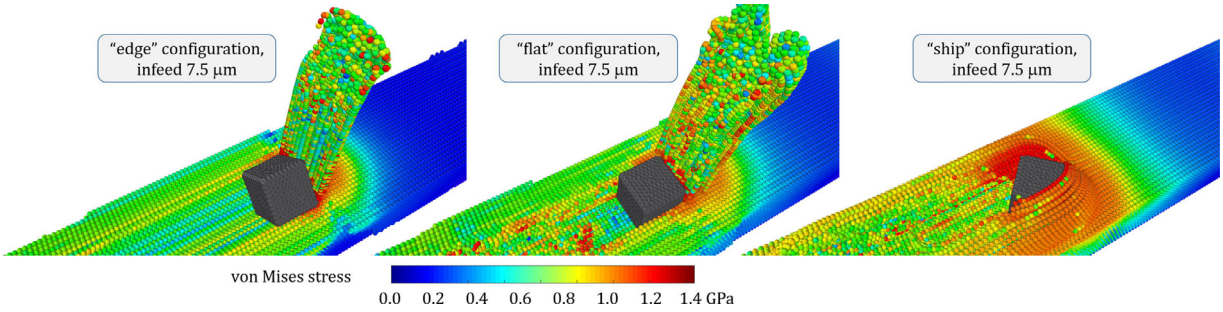

Fig. 9. MPM simulation of a grinding process of AISI 4340 steel using a single cubic abrasive. The colors of the elements correspond to the von Mises stress. At constant maximum infeed depth of 7.5μm, the panels show the difference between chip formation and plowing depending on the orientation of the abrasive.

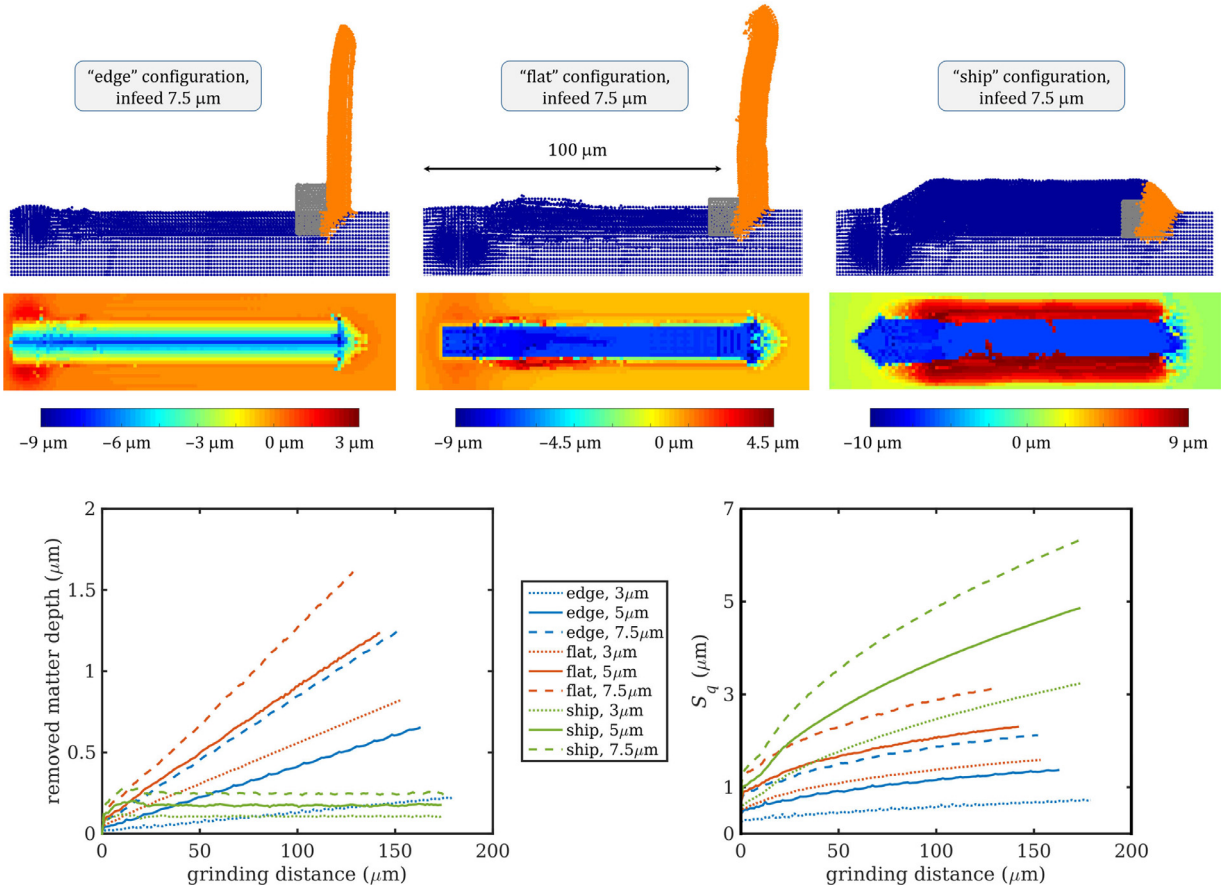

Fig. 10. MPM results overview. The top row shows representative side-views of grinding with three different abrasive configurations at the same grinding distance and infeed depth. The work piece is blue, the automatically identified chip orange, and the abrasive gray. The center row shows the corresponding topographic top view. Note that the colorbars are scaled differently to maximize contrast. The bottom row shows the removed matter depth and the RMS roughness S_q over grinding distance for all studied MPM simulations. (For interpretation of the references to color in this figure legend, the reader is referred to the web version of this article.)

shape the chip has depending on the abrasive orientation. Moreover, it shows the von Mises stress, which varies between 0 and 1.4 GPa. The largest chip is formed when the cube is sliding on one of its faces ("flat"), while no chip formation takes place at all when the abrasive is plowing through the work piece in "ship" configuration. There, the material does not pile up in front of the abrasive but flows around it, leaving a ridge on each side. As real abrasives feature a large range of natural or specially designed shapes, finding the optimal abrasive geometry and orientation within the binder will create surfaces of higher quality and, incorporating the observations made earlier, can even facilitate generating a desired microstructure near the work piece surface.

After this first, purely qualitative assessment, we went on to analyze the chip formation, material removal, and the developing surface topography in a similar fashion to how it was done for the MD systems. The first aspect of this is again the correct identification of the forming chip. Fortunately, the MPM elements are not subject to thermal oscillations, and the chips do not sway while they form, so that it is sufficient to define all elements as a part of a chip that are currently moving faster than half the grinding velocity, see the examples after approximately half the simulation time at infeed depth 7.5 m shown in the top row of Fig. 10. Note that here it is also not necessary to keep any element that was once part of a chip in that state until the end of the simulation, as the chips do not have enough time to tip over and reintegrate into the surface. Moreover, the ridges formed by the plowing abrasive in the ship configuration (top right panel) would thus be erroneously considered part of a chip.

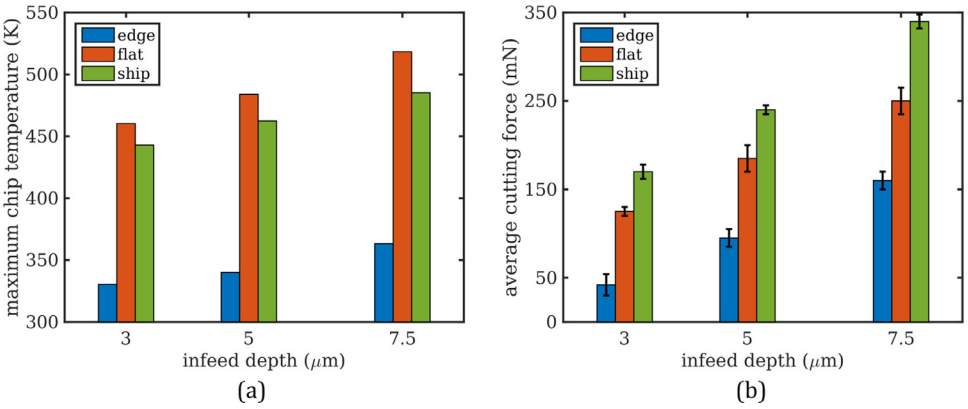

Fig. 11. (a) Maximum of the median chip temperature and (b) average cutting force as a function of infeed depth.

After having excluded the formed chip as well as the abrasive from our consideration, a meshed representation of the surface is produced, see the center row of Fig. 10. To avoid sampling artifacts, the surface mesh size was set to 30/29 of the element size, so that every mesh element has at least one MPM element within its lateral extent. Then the upper boundary of the MPM element with the highest z-component within each surface element is considered the location of the surface at that lateral position.

By producing time-resolved data series of the chip volume and the work piece surface, we can calculate an averaged removed matter depth and the RMS work piece roughness S_q as functions of time, see the bottom row of Fig. 10, which correspond to the respective plots in Figs. 4 and 5, only that the axis labels are now in m rather than nm. In the MPM simulations the grinding progress does not reach the stage where the amount of removed matter saturates, which would require the passing of several abrasives across a given work piece region. These plots must therefore be compared to the first ~ 40 nm of grinding of the steel work piece in Fig. 5, where the increase in the amount of removed matter is still linear and which was also ground at constant infeed depth of 3.0 nm. The plowing abrasive in "ship" configuration is an exception, as it does not really form a stable chip but rather must accelerate work piece material to form the parallel topographic ridges that remain attached to the work piece, which will also affect any following abrasives that were not considered in this simulation. Therefore, in the special case of the "ship" configuration, there is regardless of the infeed depth almost no removal of material but a strong (even the highest) increase in surface roughness. Both other abrasive orientations feature constant material removal rates, which are the slopes of the straight lines in the bottom left panel of Fig. 10 and can be directly compared to the slopes in the respective panels of Figs. 4 and 5 because they are non-dimensional. In general it can be stated that for all abrasive configurations, in agreement with the previous MD results, higher efficiency in terms of material removal rate results in lower surface quality. It should be noted that all of the simulated systems feature configurations leading to material removal rates of around 0.01–0.02 m/m (or nm/nm, or m/m for that matter) although our smallest and largest considered systems differ by 4 orders of magnitude in size along a given linear dimension. Similar statements can be made for the RMS roughness of the work piece when taking into account the size of the abrasive grains. A typical simulation will lead to a maximum RMS roughness of 0.1–0.2 times the abrasive size, regardless of the simulation approach, with the notable exceptions of the plowing MPM abrasive and the formation of a horizontal ridge at the highest loads in the MD ferrite system.

In addition to the aspects addressed above, we also calculated the maximum values of a typical (median) chip temperature for all abrasive orientations and infeed depths simulated with MPM, as well as the corresponding average cutting forces (forces in grinding direction), see Fig. 11. While a grinding tool designer would probably attempt to avoid the "ship" configuration of the abrasive because of a complete absence of material removal and by far the worst surface quality, these two plots show that it also leads to considerable heating in the area where the chip is formed and to the highest cutting forces. By contrast, the "edge" configuration seems to be the best compromise between decent material removal, the best surface quality, a low cutting force, and by far the lowest chip temperature. A break-down of the lateral force into components of rubbing, cutting, and plowing as proposed in [22] may shed additional light on energetic efficiency aspects of grinding in future work.

4. Conclusions

In this work, we have introduced and showcased three related meshless simulation methods to model a grinding process, spanning relevant length scales ranging from the grain diameters of nanocrystalline work pieces (<10 nm) up to sub-mm work piece extents and RMS surface roughness exceeding 5 m. All approaches explored in this work in principle allow the analysis of material removal, surface quality, grinding forces, stress and temperature distributions in the work piece, as well as the implementation of a wide range of process conditions. However, each of the methods features some advantages and disadvantages compared to the others that we list in the following:

- Atomistic MD simulation of a carbon steel work piece has the advantage of explicitly representing hard phases in the material and therefore offering an outlook of the most accurate work piece description. On the other side, this approach is computationally very expensive, meaning that the system size must be adequately reduced, which limits comparability to real processes and will usually lead to a nanocrystalline work piece that behaves differently from a microstructural point of view.
- Large-scale MD of a ferrite work piece has the advantage that it features explicit grains, large enough to qualitatively behave like a real-life material so that microstructural aspects can be thoroughly studied. However, this system does not have explicit hard phases, limiting the comparability to industrially relevant component materials. Though much larger than the steel system, it is still quite small for direct comparison to experiments and real processes.
- The mesoscopic MPM simulations of an AISI 4340 steel work piece have the advantage of representing a real component material, and its native length scale allows direct comparison to industrially mandated tolerances, while being computationally relatively cheap. On the other side, no microstructural information is considered, so effects based on the grain structure or anisotropy cannot be studied. It is also cumbersome to implement periodic boundary conditions, making it difficult to observe the saturation of the grinding process to a steady operational state.
- A load-controlled grinding process focuses on the initial moments of a real grinding process and offers the possibility to obtain typical material removal rates for sets of process conditions. This means

that such a grinding process is usually far from steady state. In combination with small system sizes, this approach limits the ability of calculating an optimum achievable surface quality.
- By contrast, an infeed controlled grinding process best represents a grinding process close to its steady state and offers the possibility to assess the final surface quality. However, the non-linear saturation behavior of the removed matter depth leads to difficulties in defining material removal rates.

What is perhaps most surprising is that, although our simulations span a range of almost 4 orders of magnitude in terms of linear length scale, the obtained material removal rates as well as the surface roughness parameters (normalized by the abrasive grain size) overlap to a remarkable extent. Therefore, our mesh-free multiscale approach to modeling grinding presented in this work may be applied to optimize numerous aspects of the process, e.g., the tweaking of grinding tool properties and process parameters to obtain a desired work piece microstructure, or finding the best balance between material removal, ground surface quality, and energy consumption.

Declaration of Competing Interest

The authors declare that they have no known competing financial interests or personal relationships that could have appeared to influence the work reported in this paper.

Acknowledgments

This work was funded by the Austrian Research Promotion Agency FFG (Project SyFi, no. 864790). Part of this work was funded by the Austrian COMET-Program (Project K2 InTribology1, no. 872176) and carried out at the “Excellence Centre of Tribology”. The computational results presented have been achieved in part using the Vienna Scientific Cluster (VSC). The government of Lower Austria is gratefully acknowledged for financially supporting the endowed professorship tribology at the TU Wien (Grant no. WST3-F-5031370/001-2017) in collaboration with AC2T research GmbH. The authors acknowledge the TU Wien Bibliothek for financial support through its Open Access Funding Program.

References

[1] Arrazola PJ, Özel T, Umbrello D, Davies M, Jawahir IS. Recent advances in modelling of metal machining processes. CIRP Ann 2013;62(2):695–718.
[2] Malkin S, Guo C. Grinding technology: theory and application of machining with abrasives. Industrial Press Inc; 2008.
[3] Wegener K, Bleicher F, Krajnik P, Hoffmeister H-W, Brecher C. Recent developments in grinding machines. CIRP Ann 2017;66(2):779–802.
[4] Rowe WB. Towards high productivity in precision grinding. Inventions 2018;3(2):24.
[5] Denkena B, Tönshoff HK. Spanen: Grundlagen. Springer-Verlag; 2011.
[6] Liu B, Xu Z, Chen C, Li R, Wang C, Yang X. In situ experimental study on material removal behaviour of single-crystal silicon in nanocutting. Int J Mech Sci 2019;152:378–83.
[7] Bai J, Bai Q, Tong Z, Guo H. Theoretical model for subsurface microstructure prediction in micro-machining ti-6al-4v alloy–experimental validation. Int J Mech Sci 2018;148:64–72.
[8] Klocke F. Fertigungsverfahren 2: Zerspanung mit geometrisch unbestimmter Schneide. Springer-Verlag; 2018.
[9] Malkin S, Guo C. Thermal analysis of grinding. CIRP Ann 2007;56(2):760–82.
[10] Grützmacher PG, Gachot C, Eder SJ. Visualization of microstructural mechanisms in nanocrystalline ferrite during grinding. Materials & Design 2020;195:109053.
[11] Zhou K, Ding HH, Wang WJ, Wang RX, Guo J, Liu QY, et al. Tribol Int 2019;134:417–26.
[12] Li P, Chen S, Xiao H, Chen Z, Qu M, Dai H, et al. Effects of local strain rate and temperature on the workpiece subsurface damage in grinding of optical glass. Int J Mech Sci 2020;182:105737.
[13] Dai C, Ding W, Xu J, Fu Y, Yu T. Influence of grain wear on material removal behavior during grinding nickel-based superalloy with a single diamond grain. Int J Mach Tools Manuf 2017;113:49–58.
[14] He CL, Zong WJ, Zhang JJ. Influencing factors and theoretical modeling methods of surface roughness in turning process: state-of-the-art. Int J Mach Tools Manuf 2018;129:15–26.
[15] Zitt U.R. Modellierung und Simulation von Hochleistungsschleifprozessen. 1999. PhD thesis, Univ., Lehrstuhl für Fertigungstechnik und Betriebsorganisation.
[16] Steffens K. Thermomechanik des Schleifens. VDI-Verlag; 1983.
[17] Fang FZ, Wu H, Liu YC. Modelling and experimental investigation on nanometric cutting of monocrystalline silicon. Int J Mach Tools Manuf 2005;45(15):1681–6.
[18] Grützmacher PG, Rammacher S, Rathmann D, Motz C, Mücklich F, Suarez S. Interplay between microstructural evolution and tribo-chemistry during dry sliding of metals. Friction 2019;7(6):637–50.
[19] Hashimoto F, Yamaguchi H, Krajnik P, Wegener K, Chaudhari R, Hoffmeister H-W, et al. Abrasive fine-finishing technology. CIRP Ann 2016;65(2):597–620.
[20] Khorasani AM, Yazdi MRS, Safizadeh MS. Analysis of machining parameters effects on surface roughness: a review. Int J Comput Mater Sci Surf Eng 2012;5(1):68–84.
[21] Brinksmeier E, Aurich JC, Govekar E, Heinzel C, Hoffmeister H-W, Klocke F, Peters J, Rentsch R, Stephenson DJ, Uhlmann E, et al. Advances in modeling and simulation of grinding processes. CIRP Annals-Manufacturing Technology 2006;55(2):667–96.
[22] Li HN, Yu TB, Wang ZX, Zhu LD, Wang WS. Detailed modeling of cutting forces in grinding process considering variable stages of grain-workpiece micro interactions. Int J Mech Sci 2017;126:319–39.
[23] Jackson MJ. Recent advances in ultraprecision abrasive machining processes. SN Applied Sciences 2020;2:1172.
[24] Goel S, Luo X, Agrawal A, Reuben RL. Diamond machining of silicon: a review of advances in molecular dynamics simulation. Int J Mach Tools Manuf 2015;88:131–64.
[25] Markopoulos AP, Karkalos NE, Papazoglou E-L. Meshless methods for the simulation of machining and micro-machining: a review. Arch Comput Methods Eng 2020;27(3):831–53.
[26] Eder SJ, Cihak-Bayr U, Bianchi D. Single-asperity contributions to multi-asperity wear simulated with molecular dynamics. IOP Conference Series: Materials Science and Engineering 2016;119(1):012009.
[27] Eder SJ, Cihak-Bayr U, Vernes A, Betz G. Evolution of topography and material removal during nanoscale grinding. J Phys D Appl Phys 2015;48:465308.
[28] Pei QX, Lu C, Lee HP, Zhang YW. Study of materials deformation in nanometric cutting by large-scale molecular dynamics simulations. Nanoscale Res Lett 2009;4(5):444–51.
[29] Meng B, Yuan D, Xu S. Study on strain rate and heat effect on the removal mechanism of sic during nano-scratching process by molecular dynamics simulation. Int J Mech Sci 2019;151:724–32.
[30] Agrawal PM, Raff LM, Bukkapatnam S, Komanduri R. Molecular dynamics investigations on polishing of a silicon wafer with a diamond abrasive. Appl Phys A 2010;100(1):89–104.
[31] Zhong J, Shakiba R, Adams JB. Molecular dynamics simulation of severe adhesive wear on a rough aluminum substrate. J Phys D Appl Phys 2013;46(5):055307.
[32] Li J, Guo J, Luo H, Fang Q, Wu H, Zhang L, et al. Study of nanoindentation mechanical response of nanocrystalline structures using molecular dynamics simulations. Appl Surf Sci 2016;364:190–200.
[33] Li J, Liu B, Luo H, Fang Q, Liu Y, Liu Y. A molecular dynamics investigation into plastic deformation mechanism of nanocrystalline copper for different nanoscratching rates. Comput Mater Sci 2016;118:66–76.
[34] Eder SJ, Cihak-Bayr U, Bianchi D. Large-scale molecular dynamics simulations of nanomachining. Advanced Machining Processes: Innovative Modeling Techniques 2017:141.
[35] Eder SJ, Ripoll MR, Cihak-Bayr U, Dini D, Gachot C. Unraveling and mapping the mechanisms for near-surface microstructure evolution in cuni alloys under sliding. ACS Applied Materials & Interfaces 2020;12(28):32197–208.
[36] Varga M, Leroch S, Eder SJ, Ripoll MR. Meshless microscale simulation of wear mechanisms in scratch testing. Wear 2017;376:1122–9.
[37] Varga M, Leroch S, Eder SJ, Rojacz H, Ripoll MR. Influence of velocity on high-temperature fundamental abrasive contact: a numerical and experimental approach. Wear 2019;426:370–7.
[38] Leroch S, Eder SJ, Ganzenmüller G, Murillo L, Ripoll MR. Development and validation of a meshless 3d material point method for simulating the micro-milling process. J Mater Process Technol 2018;262:449–58.
[39] Wang Z, Yu T, Wang X, Zhang T, Zhao J, Wen PH. Grinding temperature field prediction by meshless finite block method with double infinite element. Int J Mech Sci 2019;153:131–42.
[40] Plimpton SJ. Fast parallel algorithms for short-range molecular dynamics. J Comput Phys 1995;117:1–19.
[41] Stukowski A, Albe K. Extracting dislocations and non-dislocation crystal defects from atomistic simulation data. Modell Simul Mater Sci Eng 2010;18(8):085001.
[42] Groeber MA, Jackson MA. Dream.3d: a digital representation environment for the analysis of microstructure in 3D. Integrating Materials and Manufacturing Innovation 2014;3(1):5.
[43] Eder SJ, Bianchi D, Cihak-Bayr U, Gkagkas K. Methods for atomistic abrasion simulations of laterally periodic polycrystalline substrates with fractal surfaces. Comput Phys Commun 2017;212:100–12.
[44] Eder SJ, Cihak-Bayr U, Bianchi D, Feldbauer G, Betz G. Thermostat influence on the structural development and material removal during abrasion of nanocrystalline ferrite. ACS Applied Materials & Interfaces 2017;9(15):13713–25.
[45] Mendelev MI, Han S, Srolovitz DJ, Ackland GJ, Sun DY, Asta M. Development of new interatomic potentials appropriate for crystalline and liquid iron. Philos Mag 2003;83:3977–94.
[46] Henriksson KOE, Nordlund K. Simulations of cementite: an analytical potential for the fe-c system. Physical Review B 2009;79(14):144107.
[47] Guziewski M, Coleman SP, Weinberger CR. Atomistic investigation into interfacial effects on the plastic response and deformation mechanisms of the pearlitic microstructure. Acta Mater 2019;180:287–300.
[48] Steffan M, Haas F, Spenger T. RPM-Synchronous Grinding — Control concepts to improve surface qualities for a highly efficient non-circular grinding approach. In ASME 2017 International Mechanical Engineering Congress and Exposition, page V002T02A009 American Society of Mechanical Engineers 2017.

[49] Spenger T, Haas F, Cihak-Bayr U, Eder SJ, Weiß M, Weinzerl M, et al. RPM-Synchronous Grinding — investigation and comparison of surface topography of Synchro-Finish manufactured workpieces. Procedia CIRP 2019;81:476–81.
[50] Johnson GR, Cook WH. Fracture characteristics of three metals subjected to various strains, strain rates, temperatures and pressures. Eng Fract Mech 1985;21(1):31–48.
[51] Afazov SM, Ratchev SM, Segal J. Modelling and simulation of micro-milling cutting forces. J Mater Process Technol 2010;210(15):2154–62.
[52] Eder SJ, Feldbauer G, Bianchi D, Cihak-Bayr U, Betz G, Vernes A. Applicability of macroscopic wear and friction laws on the atomic length scale. Phys Rev Lett 2015;115:025502.
[53] Xiao G, To S, Zhang G. Molecular dynamics modelling of brittle–ductile cutting mode transition: case study on silicon carbide. Int J Mach Tools Manuf 2015;88:214–22.
[54] Denkena B, Köhler J, Kästner J. Chip formation in grinding: an experimental study. Prod Eng 2012;6(2):107–15.
[55] Eder SJ, Cihak-Bayr U, Gachot C, Ripoll MR. Interfacial microstructure evolution due to strain path changes in sliding contacts. ACS Applied Materials & Interfaces 2018;10(28):24288–301.
[56] Kelchner CL, Plimpton SJ, Hamilton JC. Dislocation nucleation and defect structure during surface indentation. Phys Rev B 1998;58(17):11085–8.
[57] Duan N, Yu Y, Wang W, Xu X. Analysis of grit interference mechanisms for the double scratching of monocrystalline silicon carbide by coupling the fem and sph. Int J Mach Tools Manuf 2017;120:49–60.
[58] Rowe WB. Principles of modern grinding technology. William Andrew 2013:86.
[59] Holtermann R, Schumann S, Menzel A, Biermann D. Modelling, simulation and experimental investigation of chip formation in internal traverse grinding. Prod Eng 2013;7(2–3):251–63.